Environmental Science Nano

ROYAL SOCIETY OF CHEMISTRY

PAPER

View Article Online
View Journal | View Issue

Cite this: *Environ. Sci.: Nano*, 2024, **11**, 336

Unveiling the origin of the efficient photocatalytic degradation of nitazoxanide over bismuth (oxy) iodide crystalline phases†

Mirabbos Hojamberdiev, *[a] Ronald Vargas, [bc] Lorean Madriz, [bc] Kunio Yubuta,[d] Zukhra C. Kadirova, [ef] Ulugbek Shaislamov, [g] Lokesh Koodlur Sannegowda, [h] Katarzyna Jędruchniewicz,[i] Rafał Typek,[j] Katsuya Teshima [k] and Bożena Czech*[i]

Received 17th August 2023,
Accepted 30th November 2023

DOI: 10.1039/d3en00548h

rsc.li/es-nano

Conventional wastewater treatment has been found to be ineffective at fully removing various antiviral drugs and emerging pollutants from wastewater. As an advanced oxidation process, heterogeneous photocatalysis is promising for detoxifying such water pollutants due to its mild operating conditions and efficiency. In this study, we explore the oxidative phase transition from bismuth iodide to bismuth oxyiodides by altering the temperature and time of thermal treatment. The influence of the temperature change from 350 °C to 450 °C on the phase transition from bismuth iodide to bismuth oxyiodides is more pronounced compared with the impact of time. This results in the formation of different bismuth oxyiodide crystalline phases with varying optoelectronic properties and photocatalytic activity. The effect of the bismuth iodide-to-bismuth oxyiodide phase transition on the efficiency of the photocatalytic removal of nitazoxanide is investigated in this study. The significant role of the BiOI/$Bi_4O_5I_2$ heterostructure is established in facilitating the rapid photocatalytic degradation of nitazoxanide, with respective rate constants of k_1 (0.051 min^{-1}) and k_2 (4.225 mg g^{-1} min^{-1}) obtained for the photocatalyst sample thermally treated at 375 °C for 1 h. Trapping experiments provide evidence that photoexcited holes and hydroxyl

Environmental significance

Nitazoxanide is categorized as a pharmaceutical compound possessing both antiparasitic and antibacterial attributes. Despite its cost-effectiveness, the extensive use of nitazoxanide for treating various diseases has resulted in the detection of its traces in wastewater due to its poor permeability and solubility. Conventional wastewater treatment methods have proven to be ineffective in fully eliminating various antiviral drugs and emerging pollutants from wastewater. Heterogeneous photocatalysis, an advanced oxidation process, is promising for the decontamination of such waterborne pollutants due to its efficient performance under mild operational conditions. This study investigates the impact of thermal treatment on the transition from bismuth iodide to bismuth oxyiodides and the efficacy of photocatalytic removal of nitazoxanide. The BiOI/$Bi_4O_5I_2$ heterostructure exhibits the highest efficiency in photocatalytic removal of nitazoxanide. Assessment of toxicity using *Aliivibrio fischeri* demonstrates that the BiOI/$Bi_4O_5I_2$ heterostructure is effective not only in photocatalytic removal of nitazoxanide but also in wastewater detoxification. This underscores its potential for practical application within wastewater treatment processes.

[a] *Institut für Chemie, Technische Universität Berlin, Straße des 17. Juni 135, 10623 Berlin, Germany. E-mail: hmirabbos@gmail.com*
[b] *Instituto Tecnológico de Chascomús (INTECH), Consejo Nacional de Investigaciones Científicas y Técnicas (CONICET), Universidad Nacional de San Martín (UNSAM), Avenida Intendente Marino, Km 8,2, (B7130IWA), Chascomús, Provincia de Buenos Aires, Argentina*
[c] *Escuela de Bio y Nanotecnologías, Universidad Nacional de San Martín (UNSAM), Avenida Intendente Marino, Km 8,2, (B7130IWA), Chascomús, Provincia de Buenos Aires, Argentina*
[d] *Department of Applied Quantum Physics and Nuclear Engineering, Kyushu University, Fukuoka 819-0395, Japan*
[e] *Department of General and Inorganic Chemistry, Faculty of Chemistry, National University of Uzbekistan, University Street 4, 100174 Tashkent, Uzbekistan*
[f] *Uzbekistan-Japan Innovation Center of Youth, University Street 2B, 100095 Tashkent, Uzbekistan*
[g] *Center for Development of Nanotechnology at the National University of Uzbekistan, Tashkent, Uzbekistan, University str. 4, 100174 Tashkent, Uzbekistan*
[h] *Department of Studies in Chemistry, Vijayanagara Sri Krishnadevaraya University, Cantonment, Vinayakanagara, Ballari, 583105, India*
[i] *Department of Radiochemistry and Environmental Chemistry, Institute of Chemical Sciences, Faculty of Chemistry, Maria Curie-Skłodowska University in Lublin, 3 Maria Curie-Skłodowska Sq., 20-031 Lublin, Poland. E-mail: bozena.czech@mail.umcs.pl*
[j] *Department of Chromatography, Institute of Chemical Sciences, Faculty of Chemistry, Maria Curie-Skłodowska University in Lublin, 3 Maria Curie-Skłodowska Sq., 20-031 Lublin, Poland*
[k] *Department of Materials Chemistry, Shinshu University, 4-17-1 Wakasato, Nagano 380-8553, Japan*

† Electronic supplementary information (ESI) available. See DOI: **https://doi.org/10.1039/d3en00548h**

radicals play a crucial role in the photocatalytic degradation of nitazoxanide. The photodegradation of nitazoxanide in aqueous solution over crystalline bismuth (oxy)iodide proceeds *via* hydrolysis into acetylsalicylic acid and the respective aminonitrothiazol, followed by the deacetylation and decarboxylation processes. Molecular dynamics simulation confirms that the high photocatalytic activity of BiOI/$Bi_4O_5I_2$ is correlated to the higher adsorption energy due to the formation of a network of close contacts (<3.5 Å) between nitazoxanide molecules and iodine atoms.

1. Introduction

The increasing world population and the surge in various viral infections causing either an epidemic or a pandemic are leading to the development and usage of new types of antiviral drugs. As an emerging class of anthropogenic pollutants, these antiviral drugs are reaching the environment and affecting human health.[1] Recent studies have revealed that antiviral drugs can travel through wastewater treatment plants with varying degrees of biotransformation, and residues of antiviral drugs have been observed in wastewater effluent,[2] surface water,[3] and also groundwater.[4] Despite their relatively low environmental concentrations (ng L^{-1} to μg L^{-1}) and natural attenuation by photolysis, hydrolysis, sorption, and biodegradation, the continuous discharge of these antiviral drugs poses a significant risk to bio-organisms and could lead to the formation of antiviral-resistant strains.[5,6] Unfortunately, conventional wastewater treatment plants do not effectively remove antiviral drugs by existing water treatment technologies.[7] Therefore, advanced water treatment processes must be developed to completely remove these antiviral drugs.

Among the advanced oxidation processes, heterogeneous photocatalysis holds promise for effectively removing antiviral drugs and other emerging water pollutants thanks to its *in situ* generation of reactive species, efficiency, stability, recoverability, reusability, low energy consumption, mild operating conditions, and cost-effectiveness.[8] Previously, we used SnO_2@ZnS,[9] elsmoreite/tungsten oxide@ZnS,[10] and industrial waste-derived multiphase photocatalysts[11] to effectively remove various selected pharmaceuticals and antiviral drugs from the contaminated model and real wastewater and explored the toxicity of the photocatalytically treated lopinavir- and ritonavir-containing water and wastewater.[12] Wang *et al.*[13] studied the photodegradation of oseltamivir phosphate using TiO_2-P25 and found that although >95% was removed after 80 min of UV-A irradiation, the removal efficiency of total organic carbon was only 45.6–67.0%. Various α-Fe_2O_3-based heterostructures favor the photodegradation of sulfamethoxazole, bisphenol-A, tetracycline hydrochloride, norfloxacin, salicylic acid, carbamazepine, metronidazole, tetracycline, and lomefloxacin with efficiencies in the range of >80% to 100%.[14]

As photocatalytic materials, layered compounds have the potential for solar energy conversion and environmental remediation because of their unique layered crystal structure, favorable electronic band structure, diverse composition, and rich atomic coordination.[15] Having a layered structure comprising $[Bi_2O_2]^{2+}$ layers interleaved by slabs of iodine atoms, bismuth oxyiodides ($Bi_xO_yI_z$) are visible-light-active photocatalysts with optical bandgap energies in the range of 1.8–2.9 eV.[16] The open, layered structure of $Bi_xO_yI_z$ not only favors the separation and transfer of photoexcited charge carriers due to the internal electrostatic field vertical to the layer direction but also reduces the surface trapping of photoexcited charge carriers.[17–19] The substitution of more I atoms by O atoms in the $Bi_xO_yI_z$ lattice leads to the formation of other members: BiOI, $Bi_4O_5I_2$, α-Bi_5O_7I, β-Bi_5O_7I, and $Bi_7O_9I_3$, which exhibit different optoelectronic properties and photocatalytic activities.[20] BiOI single crystal nanosheets with dominant exposed {001} facets were synthesized by annealing BiI_3 at 280 °C for 16 h, and the {001} facet-dependent photocatalytic activity for the degradation of rhodamine B was seven times higher than that of irregular BiOI.[21] The spherical microstructures of orthorhombic-Bi_5O_7I were synthesized by thermal conversion of BiOI microspheres in air, and the sample thermally treated at 450 °C exhibited high photocatalytic activity for the degradation of rhodamine B due to its high crystallinity, high surface area and porous microstructure.[16] Similarly, $Bi_4O_5I_2$ nanosheets synthesized by thermal treatment of BiI_3 at 450 °C showed high photocatalytic activity for the degradation of rhodamine B and salicylic acid.[20] Despite their high photocatalytic activities for the degradation of organic dyes, bismuth oxyiodides ($Bi_xO_yI_z$) have not been studied for the degradation of antiviral drugs.

Nitazoxanide [2-acetyloxy-*N*-(5-nitro-2-thiazolyl)benzamide] ($C_{12}H_9N_3O_5S$, CAS no. 55981-09-4) is classified as a pharmaceutical substance with antiparasitic and antibacterial activity. During the COVID-19 pandemic, nitazoxanide was used as a low-cost drug, and its active metabolite can inhibit the replication of both RNA and DNA, exhibiting action against various viruses, including SARS-CoV-2 (severe acute respiratory syndrome coronavirus type 2).[22] The extensive use of nitazoxanide for treating various diseases, including cryptosporidiosis, resulted in the detection of its traces in wastewater matrices due to its persistence, which stems from its poor permeability and solubility (7.55 mg L^{-1}).[23] Therefore, it is important to find a novel approach to efficiently remove it from contaminated water and wastewater. So far, no studies have been conducted to investigate the photocatalytic removal of nitazoxanide except for *via* photolysis.[24] Therefore, the effect of the bismuth iodide-to-bismuth oxyiodide phase transition on the efficiency of the photocatalytic removal of nitazoxanide is investigated in this study. The phase transition from bismuth iodide to bismuth oxyiodides is explored by changing the temperature and time of thermal treatment. The kinetics and mechanism behind the photocatalytic removal of nitazoxanide are also presented.

2. Experimental

2.1. Preparation and characterization

Bismuth(III) iodide (99%, Merck) was thermally treated in air at temperatures in the range of 350–450 °C for 1 h and also at 350 °C for different times (1, 3, 5, 7, and 9 h). The X-ray diffraction (XRD) patterns were acquired with a PANalytical X'Pert PRO diffractometer with Cu K_α radiation. The bright-field and lattice images and selected-area electron diffraction (SAED) patterns were obtained using an EM-002B (TOPCON) high-resolution transmission electron microscope (TEM) at an accelerating voltage of 200 kV. The microstructures were observed by a Carl Zeiss Gemini 982 scanning electron microscope (SEM). The surface chemical states of elements were analyzed by X-ray photoelectron spectroscopy (XPS, JPS-9010MX, JEOL) using non-monochromatic Mg-K_α radiation. The UV-vis diffuse reflectance spectra were recorded on an Evolution 220 UV/vis spectrometer (Thermo Fisher Scientific).

The photoanodes were fabricated by depositing the synthesized bismuth (oxy)iodide powders, and the photoelectrochemical (PEC) measurements were carried out according to a protocol reported elsewhere.[25] The geometric area of the working electrode was 1.54 cm^2, the counter electrode was a Pt wire, a reference hydrogen electrode (RHE) was used, and 0.1 M Na_2SO_4 (50 mL) was employed as the supporting electrolyte. The chronoamperometry (CA) results at 1.8 V *vs.* RHE and open-circuit potential decay (OCPD) data were obtained (Princeton Applied Research PAR263 Potentiostat). Moreover, the lifetime (τ) of the carriers was calculated according to the following equation: $\tau = |k_B T/e_0 \ (dE_{OC}/dt)^{-1}|$, where E_{OC} is the open-circuit potential, t is the time, k_B is the Boltzmann potential constant, T is the absolute temperature, and e_0 is the elemental charge.[26] Irradiation was provided by a Newport solar simulator (150 W Xe lamp), and the light photon flux was set to 100 mW cm^{-2}.

2.2. Photocatalytic activity tests

The photocatalytic activity of the photocatalyst samples for the degradation of nitazoxanide was evaluated. First, 0.4 mg L^{-1} of the photocatalyst sample was dispersed in an aqueous solution of nitazoxanide (10 mg L^{-1}) in a photochemical reactor (0.7 L, Heraeus) in the dark for 30 min to achieve adsorption–desorption equilibrium. Then, a 150 W mercury lamp, which was vertically placed in the center of the photoreactor, with emitting radiation centered at 500–550 nm, an intensity of 7.31–7.53 mW cm^{-2}, and a photon flux of 20.83×10^{19} m^2 s^{-1}, was turned on. Aliquots were collected at various times before and during the photocatalytic reaction (−30, 0, 5, 15, 30, 45, 60, and 120 min) and filtered. The collected aliquots were analyzed using an Agilent 1260 Infinity II LC-DAD chromatograph equipped with an InfinityLab Poroshell 120 EC-C18 column (3.0 × 150 mm, 2.7 μm), using H_2O + CH_3COONH_4 (pH = 6) : ACN (v/v 60 : 40) as the mobile phase (flow 0.5 mL min^{-1}, temperature 30 °C), and analyzed at λ_{NTZ} = 240 nm, R_T = 3.99 min. The fitting of the calibration curve was R^2 = 0.9998. The ratio of the nitazoxanide concentrations before and after the photocatalytic reactions, C/C_0, was used to indicate the amount of nitazoxanide that had been photocatalytically removed from the aqueous solution.

The chromatographic analysis of by-products was performed using an LC/MS system consisting of an ultra-high-performance liquid chromatograph (UltiMate 3000, Thermo Fisher Scientific) connected with a linear trap quadrupole-Orbitrap mass spectrometer (LTQ-Orbitrap Velos, Thermo Fisher Scientific) equipped with an ESI source. In all analyses, a Gemini C18 column (4.6 × 100 mm, 3 μm) (Phenomenex) was used for the chromatographic separation. During the chromatographic process, gradient elution was used. Mobile phase A was 25 mM formic acid in water, and mobile phase B was 25 mM formic acid in acetonitrile. The gradient program started at 5% B, increasing to 85% by 40 min, followed by isocratic elution at 85% B for 5 min. The total run time was 45 min at the flow rate of 0.5 mL min^{-1}. During each run, the MS spectra in the m/z range of 50–500 were continuously collected.

The effects of various parameters, such as competing ions (Cl^-, NO_3^-, and $H_2PO_4^-$ from respective sodium salts with a concentration of 5×10^{-3} mol L^{-1}) and water matrices (distilled water [DW], tap water [TW], and treated wastewater [TWW]), on the efficiency of the photocatalytic degradation of nitazoxanide over the prepared samples were studied. TWW was collected from the "Hajdów" municipal wastewater treatment plant in Lublin, which is a mechanical–biological wastewater treatment facility with increased removal of biogenic compounds (nitrogen and phosphorus) from wastewater. TWW was characterized by significantly reduced biological (5.7 mg L^{-1}) and chemical (35.1 mg L^{-1}) oxygen demands, total suspended solids (up to 6.4 mg L^{-1}), and total nitrogen (10.72 mg L^{-1}) and phosphorous (0.27 mg L^{-1}) contents. TW was characterized by total organic carbon (<3 mg L^{-1}), chlorides (35 mg L^{-1}), nitrates (<2 μg L^{-1}), sulfates (41 mg L^{-1}) contents, and pH of 7.2. The reusability test was performed using the sample thermally treated at 375 °C for three repetitive cycles with an intermediate washing with ethanol and distilled water and drying at 105 °C.

To gain insights into the possible reaction mechanism for the photodegradation of nitazoxanide over the prepared samples, the trapping experiments were conducted using isopropyl alcohol (IPA, 1000 mg L^{-1}), *p*-benzoquinone (PBQ, 1 mg L^{-1}), and ethylenediaminetetraacetic acid disodium salt dihydrate (Na_2EDTA, 100 mg L^{-1}) as scavengers of $^{\bullet}OH$, $O_2^{\bullet-}$, and h^+, respectively. Toxicity towards marine bacteria (*Aliivibrio fischeri*) was evaluated based on the inhibition of bioluminescence using the Microtox® test.[27] The luminescence inhibition was determined after 5 min and 15 min of exposure of *Aliivibrio fischeri* to the water samples before and after the photocatalytic reaction according to the standard protocol (Microtox®, 1995) in a Microtox M500 analyzer using Omni software.

3. Results and discussion

3.1. Characterization of materials

The phase transition from bismuth iodide to bismuth oxyiodides was studied by changing the temperature and time of thermal treatment in air. Fig. 1a shows the XRD patterns of samples thermally treated at temperatures ranging from 350 °C to 450 °C for 1 h. The XRD pattern of the as-received bismuth iodide indicates major reflections assignable to trigonal BiI_3 with space group $R\bar{3}$ and lattice parameters of a = 7.5250 Å and c = 20.7030 Å (ICSD# 98-007-8791). In addition, minor reflections belonging to tetragonal BiOI with space group $P4/nmm$ and lattice parameters of a = 3.9950 Å and c = 9.1510 Å (ICSD# 98-039-1354) are also observed. At 350 °C, tetragonal BiOI becomes a dominating crystalline phase as a result of the evaporation of iodine and oxidation. Monoclinic $Bi_4O_5I_2$ with space group $P12_11$ and lattice parameters of a = 11.2630 Å, b = 5.6980 Å, c = 14.9440 Å, and β = 99.81° (ICSD# 98-041-2590) accompanies tetragonal BiOI in the sample thermally treated at 375 °C and turns into a dominating crystalline phase at 400 °C. At 425 °C and 450 °C, the reflections associated with monoclinic $Bi_4O_5I_2$ disappear altogether, and new reflections referable to orthorhombic Bi_5O_7I with space group $Ibca$ and lattice parameters of a = 5.3440 Å, b = 16.2650 Å, and c = 23.0200 Å (ICSD# 98-041-1666). The XRD patterns in Fig. 1b confirm that extending the time of thermal treatment at 350 °C from 1 h to 9 h led to the phase transition from trigonal BiI_3 to tetragonal BiOI first and then to monoclinic $Bi_4O_5I_2$. Evidently, the change in the temperature of the thermal treatment had a stronger impact on the phase transition than the shift in the time of the thermal treatment. Previous studies found that the oxidative conversion of BiI_3 to Bi_2O_3 occurred either through the formation of $Bi_4O_5I_2$ (and BiOI)[20] or Bi_5O_7I (and BiOI),[21] but not both. Here, by controlling the temperature of the thermal treatment, the oxidative conversion of BiI_3 proceeded according to the following stages:

$$2BiI_3 + O_2 \rightarrow 2BiOI + 2I_2\uparrow \quad (1)$$

$$8BiOI + O_2 \rightarrow 2Bi_4O_5I_2 + 2I_2\uparrow \quad (2)$$

$$10Bi_4O_5I_2 + 3O_2 \rightarrow 8Bi_5O_7I + 6I_2\uparrow \quad (3)$$

The formation of BiOI, $Bi_4O_5I_2$, and Bi_5O_7I phases allows us to understand the contribution of each crystalline phase to the efficiency of the photocatalytic degradation of nitazoxanide.

The morphological change as a consequence of the oxidative conversion of bismuth iodide was selectively observed by means of scanning electron microscopy (SEM). Fig. 2 shows the SEM images of samples before and after thermal treatment at 350 °C and 450 °C. As shown in Fig. 2a, bismuth iodide has an irregular morphology in different sizes. In contrast, the sample thermally treated at 350 °C contains plate-like structures of BiOI as a result of the oxidation of bismuth iodide and evaporation of I_2 (Fig. 2b). Interestingly, the thickness and shape of the plate-like structures of BiOI are different from those reported previously.[20,21] Presumably, such discrepancy arises from the difference in internally accumulated I_2 vapor pressure, which leads to peeling off the surface shells of BiOI layer by layer and forming ultrathin nanosheets. A further increase in the thermal treatment temperature to 450 °C resulted in the formation of layered structures of Bi_5O_7I with pores because of the accelerated release of I_2 vapor (Fig. 2c). The corresponding energy-dispersive X-ray spectroscopy (EDX) data indicate a lessening of the peak intensity of iodine due to its evaporation during thermal treatment. The surface chemical states of samples were analyzed by XPS. The XPS results for the samples thermally treated at different temperatures are shown in Fig. 3. Note that BiI_3 was not stable during the XPS analysis. In Fig. 3a, two peaks corresponding to the Bi $4f_{7/2}$ and Bi $4f_{5/2}$ states are observed at 159.4 eV and 164.7 eV, respectively, indicating the +3 oxidation state of bismuth. In the I 3d XPS spectra in Fig. 3b,

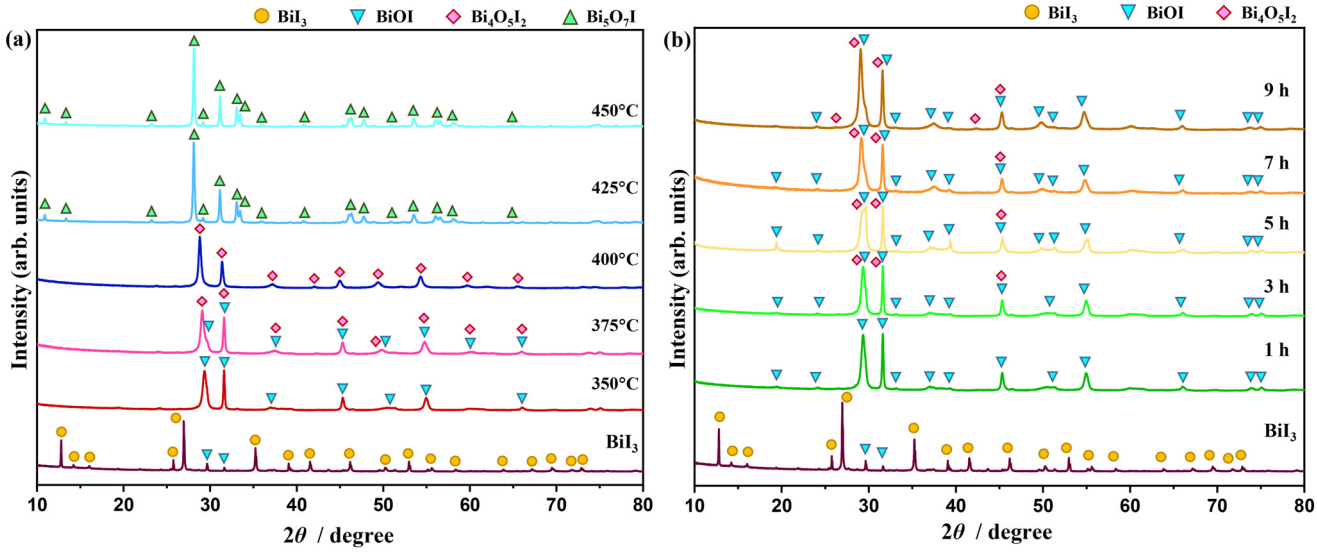

Fig. 1 XRD patterns of samples thermally treated at temperatures ranging from 350 °C to 450 °C for 1 h (a) and at 350 °C for 1–9 h (b) in air.

two peaks at 619.4 eV and 630.8 eV can be assigned to the I $3d_{5/2}$ and I $3d_{3/2}$ states, respectively, implying the −1 oxidation state of iodine. The O 1s XPS spectra in Fig. 3c can be deconvoluted into two peaks at 530.1 eV and 528.4 eV, which can be ascribed to the lattice oxygen and surface chemisorbed oxygen, respectively. Although no significant difference can be seen in the XPS spectra, the results of quantitative XPS analysis in atomic percentage confirm that the contents of bismuth and oxygen increased and the bismuth content decreased with increasing thermal treatment temperature.

Next, the nanostructural transformation as a result of the oxidative conversion of bismuth iodide was analyzed by means of transmission electron microscopy (TEM). Fig. 4 shows the bright-field TEM and HRTEM images and corresponding selected area electron diffraction (SAED) patterns of samples before and after thermal treatment at 350 °C, 400 °C, and 450 °C. The bright-field TEM images clearly indicate a smooth surface with hexagonal nanosheets for the bismuth iodide before thermal treatment, a rough surface with plate-like nanostructures for the samples thermally treated at 350 °C and 400 °C due to the phase transition, crystallization, and inception of pore formation (average pore size is about 30 nm), and plate-like nanoporous nanostructures for the sample thermally treated at 450 °C because of the increased emission of I_2 vapor. In the HRTEM images, the lattice fringes observed in the regions of the plate-like nanostructures show the *d*-spacing values of 0.303, 0.285, 0.946, and 0.832 nm, revealing the exposed (113),

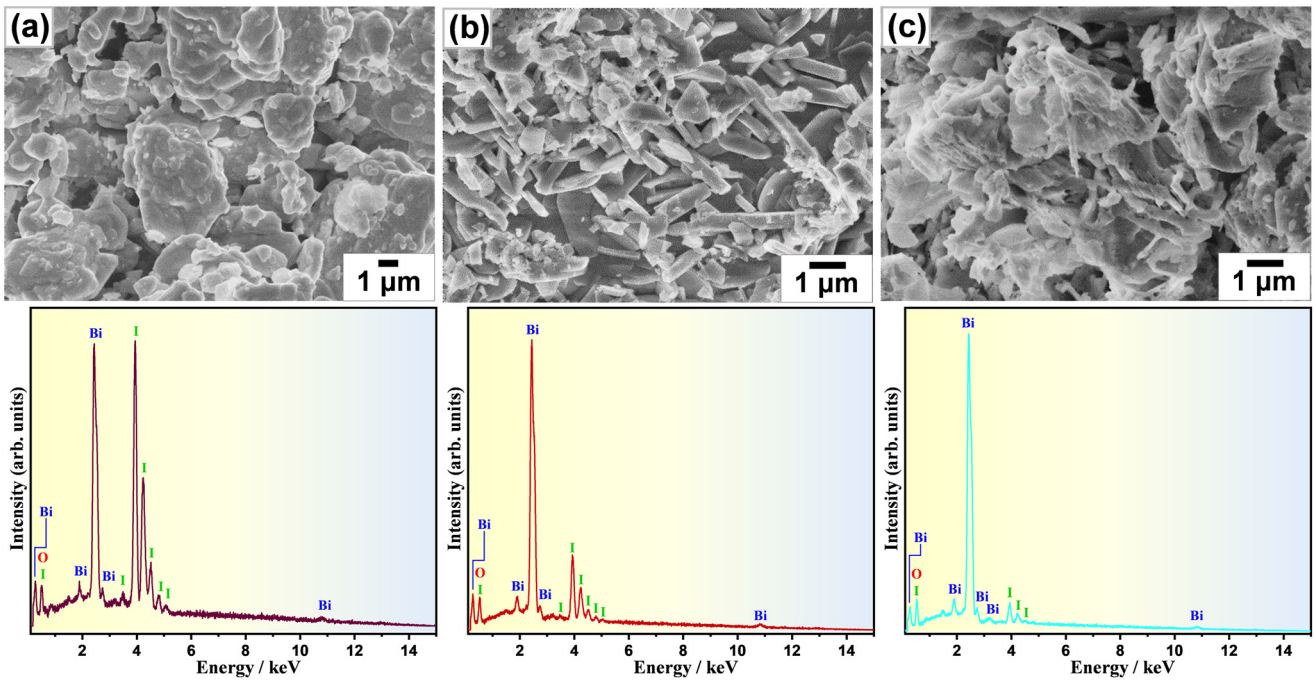

Fig. 2 SEM images and EDS spectra of samples (a) before and after thermal treatment at (b) 350 °C and (c) 450 °C for 1 h in air.

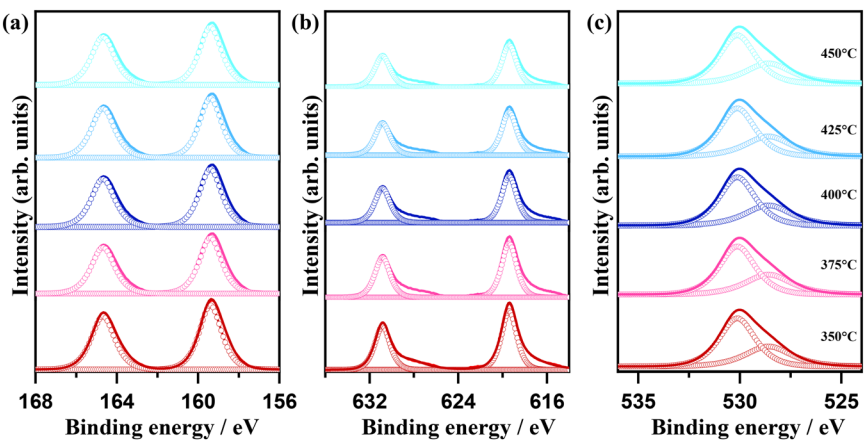

Fig. 3 (a) Bi 4f, (b) I 3d, and (c) O 1s XPS spectra of samples thermally treated at temperatures ranging from 350 °C to 450 °C for 1 h in air.

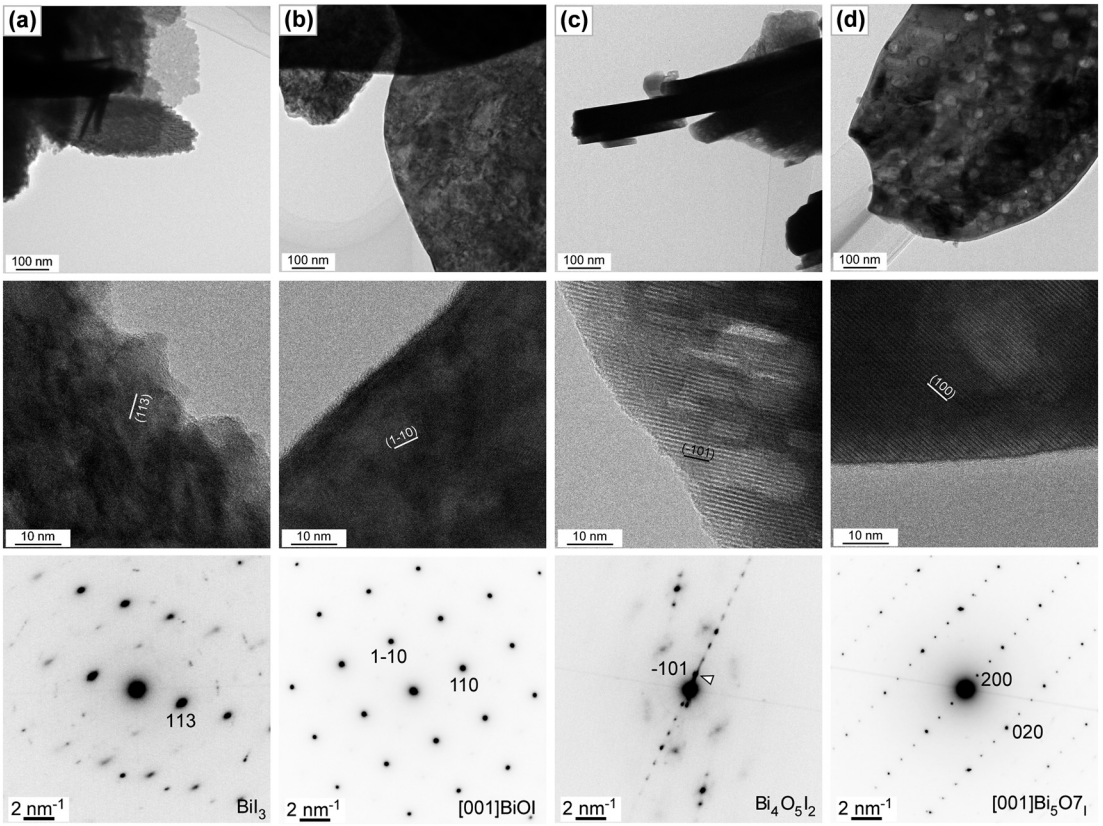

Fig. 4 TEM and HRTEM images and SAED patterns of samples (a) before and after thermal treatment at (b) 350 °C, (c) 400 °C, and (d) 450 °C for 1 h in air.

($1\bar{1}0$), ($\bar{1}01$), and (200) crystal planes of BiI_3, BiOI, $Bi_4O_5I_2$, and Bi_5O_7I, respectively. This corroborates the oxidative phase transition from bismuth iodide to bismuth oxyiodides at the nanoscale. No significant defects were observed in the analyzed areas, implying their high crystallinity. The highly ordered SAED patterns confirm the single-crystalline nature of BiI_3, BiOI, $Bi_4O_5I_2$, and Bi_5O_7I. By indexing the diffraction spots in the SAED patterns, the trigonal, tetragonal, monoclinic, and orthorhombic crystal structures of BiI_3, BiOI, $Bi_4O_5I_2$, and Bi_5O_7I were confirmed. In addition, the SEM image of the sample thermally treated at 375 °C is shown in Fig. S1 in the ESI,† indicating the formation of $BiOI/Bi_4O_5I_2$ heterostructures.

The oxidative phase transition from bismuth iodide to bismuth oxyiodides influences the optical properties. Therefore, the light absorption characteristics of the samples were analyzed by means of UV-vis absorption spectroscopy. Fig. 5 shows the UV-vis diffuse reflectance spectra of the samples. Apparently, the greyish-black color of bismuth iodide powder gradually turned into reddish-orange, orange, yellow, milky white, and white as the thermal treatment temperature increased to 450 °C, whereas the greyish-black color of bismuth iodide powder slowly changed to reddish-orange, vivid orange, and light orange with increasing time of thermal treatment at 350 °C up to 9 h. In the UV-vis diffuse reflectance spectra (Fig. 5a), the absorption edges are observed at the wavelengths of about 715, 635, 615, 520, and 388 nm, which correspond to the optical bandgap energies of 1.73, 1.95, 2.01, 2.38, and 3.19 eV, for the samples before (BiI_3) and after thermal treatment at 350 °C (BiOI), 375 °C (BiOI + $Bi_4O_5I_2$), 400 °C ($Bi_4O_5I_2$), 425 °C (Bi_5O_7I), and 450 °C (Bi_5O_7I), respectively. In contrast, the samples before and after thermal treatment at 350 °C for different times exhibit absorption edges at wavelengths of approximately 715, 639, 636, 628, 623, and 615 nm, which correspond to optical bandgap energies of 1.73, 1.94, 1.95, 1.97, 1.99, and 2.01 eV, respectively (Fig. 5b). As can be seen, most of the synthesized samples are visible light active, harvesting solar energy efficiently. A pronounced increase in the optical bandgap energy to 3.19 eV in the samples thermally treated at different temperatures is consistent with the oxidative phase transition from BiI_3 to Bi_5O_7I. A gradual blueshift in the absorption edges in the UV-vis diffuse reflectance spectra of the samples thermally treated at 350 °C for different times is in good agreement with the oxidative phase transition of BiI_3 to BiOI with increased content of $Bi_4O_5I_2$. This implies that the change in the temperature of the thermal treatment influenced the phase transition more effectively than the time change of the thermal treatment.

The effect of the oxidative conversion of bismuth iodide to bismuth oxyiodides on the photodegradation of nitazoxanide

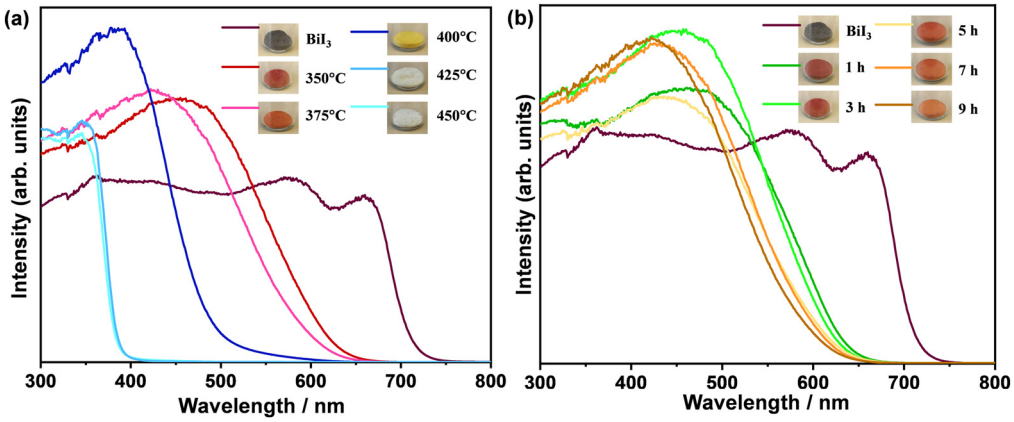

Fig. 5 UV-vis diffuse reflectance spectra of samples thermally treated (a) at temperatures ranging from 350 °C to 450 °C for 1 h and (b) at 350 °C for 1–9 h in air.

was studied. Fig. 6a and b show the change in the concentration of nitazoxanide in an aqueous solution during photocatalysis in the presence of the prepared photocatalyst samples. A previous study on the photodegradation kinetics of nitazoxanide revealed that direct UV-assisted photolysis could degrade only 30% of nitazoxanide.[24] As shown in Fig. 6a and b, the synthesized photocatalytic materials exhibited a poor adsorption capacity (<10%) for nitazoxanide (C_0 = 10 mg L^{-1}) in the dark. In Fig. 6a, even though bismuth oxide and the other two samples thermally treated at 350 °C and 400 °C showed a higher photodegradation rate for nitazoxanide in the initial stage (5–15 min), they did not completely degrade nitazoxanide. In contrast, the sample thermally treated at 375 °C fully mineralized nitazoxanide after 60 min. The samples thermally treated at 425 °C and 450 °C showed the slowest photodegradation rates for nitazoxanide. The discrepancy in the efficiency of photodegradation of nitazoxanide over the samples thermally treated at different temperatures is mainly associated with the oxidative conversion of BiI_3 to BiOI, BiOI + $Bi_4O_5I_2$, $Bi_4O_5I_2$, and Bi_5O_7I phases with different optoelectronic properties. The highest photocatalytic activity for the degradation of nitazoxanide was observed for the sample thermally treated at 375 °C due to the formation of a BiOI/$Bi_4O_5I_2$ heterostructure. Similarly, the BiOI/$Bi_4O_5I_2$ heterostructure showed a significantly higher photocatalytic activity for the degradation of methylene blue due to the efficient charge transfer and separation.[28] Despite its absorption up to 715 nm, bismuth iodide showed lower photocatalytic activity in comparison to BiOI, BiOI + $Bi_4O_5I_2$, and $Bi_4O_5I_2$ because of the presence of defects acting as the recombination centers for photoexcited charge carriers. Changing the thermal treatment time from 1 h to 9 h resulted in a less differentiated but reduced photodegradation rate because of the increased content of $Bi_4O_5I_2$ in the BiOI/$Bi_4O_5I_2$ heterostructure (Fig. 6b). As shown in Fig. 5a, $Bi_4O_5I_2$ has limited visible light absorption in comparison to BiOI. The efficiency of the BiOI/$Bi_4O_5I_2$ heterostructure in the photocatalytic removal of nitazoxanide cannot be compared with other photocatalysts due to the absence of previous studies on the photocatalytic degradation of nitazoxanide in the presence of photocatalysts. Nevertheless, the efficiency of the BiOI/$Bi_4O_5I_2$ heterostructure was compared with the efficiencies of other bismuth oxyiodides for the photocatalytic degradation of various organic compounds (Table S1†). Apparently, the BiOI/$Bi_4O_5I_2$ heterostructure exhibits higher efficiency in the photocatalytic degradation of nitazoxanide compared with the other bismuth oxyiodide compounds in Table S1.†

Various BiOI-based photocatalysts have shown high efficiency in the photocatalytic removal of different pharmaceuticals under visible light irradiation. For instance, the BiOI/UiO-66 p–n heterojunction showed nearly 100% removal efficiency for sulfadiazine (5 mg L^{-1}) within 90 min of visible light irradiation.[29] Ag-decorated BiOI applied as a counter electrode significantly enhanced the photoelectrocatalytic removal (92%) of diclofenac sodium (10 mg L^{-1}) over an Ag–$BiVO_4$/BiOI photoanode after 2 h due to the formation of a type II p–n heterojunction and a Schottky barrier.[30] The ClO_2-added BiOI-based system achieved 100% removal of sulfamethoxazole within 30 min because of the activation of chlorite to chlorine dioxide.[31] Very recently, an Fe^{III}/$BiOIO_3$ piezo-catalytic self-Fenton system was developed, which can offer exceptional self-recyclable degradation of pollutants with a degradation rate constant for sulfamethoxazole over 3.5 times that of the classic Fe^{II}-based system.[32]

The kinetics of the photocatalytic removal of nitazoxanide by the prepared photocatalysts were estimated by applying two different models: pseudo-first-order (Langmuir–Hinshelwood) and pseudo-second-order, and the results are given in Table 1 and Fig. S2a and b in the ESI.† Quantitatively, the kinetics of the photocatalytic removal of nitazoxanide by the photocatalyst samples thermally treated at different temperatures can be ascribed to both models, while the kinetics of the photocatalytic removal of nitazoxanide by the photocatalyst samples thermally treated for different times follow the pseudo-second-order. In fact,

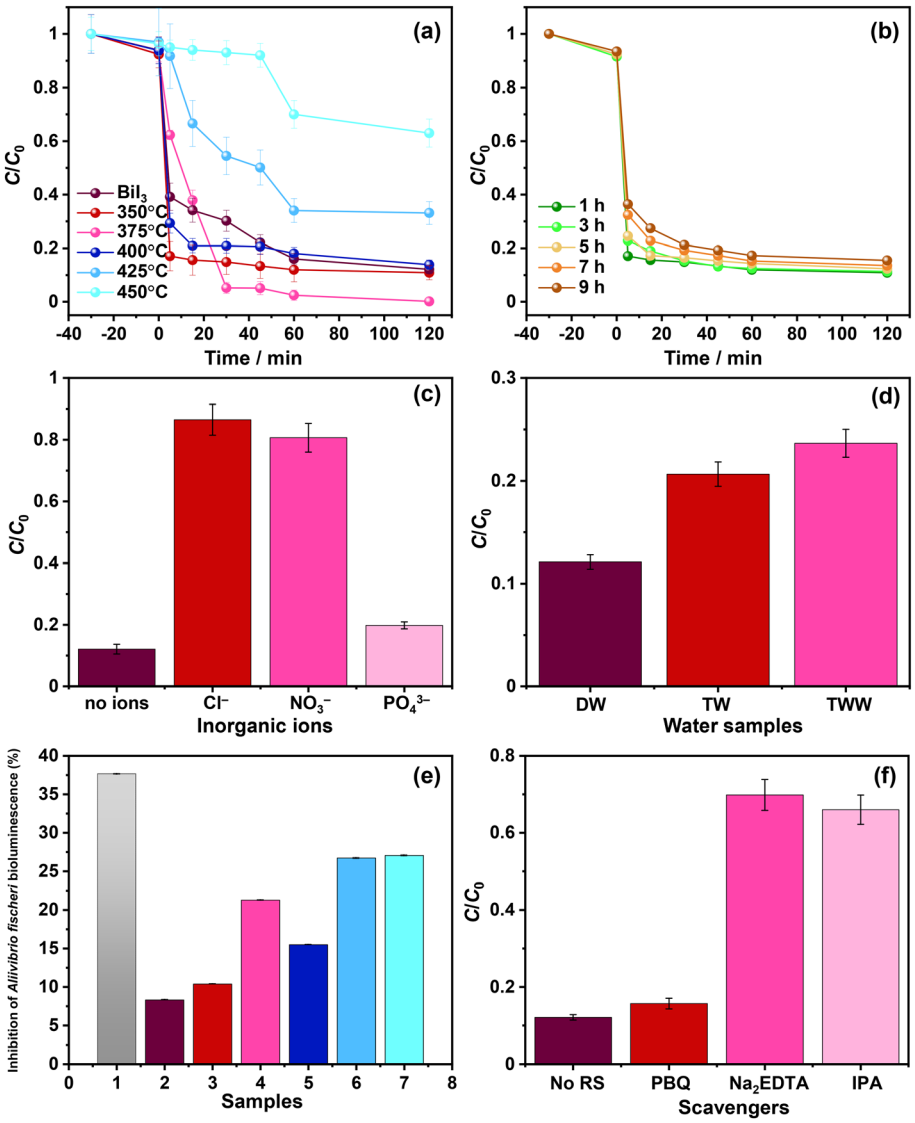

Fig. 6 Photocatalytic activity for the degradation of nitazoxanide of samples thermally treated (a) at temperatures ranging from 350 °C to 450 °C for 1 h and (b) at 350 °C for 1–9 h in air. Effects of (c) inorganic ions and (d) water matrices on the photocatalytic removal of nitazoxanide by the sample thermally treated at 375 °C for 1 h. (e) Inhibition of *Aliivibrio fischeri* bioluminescence for the water samples (1) before and after the photocatalytic treatment with samples (2) before and after thermal treatment at (3) 350 °C, (4) 375 °C, (5) 400 °C, (6) 425 °C, (7) and 450 °C. (f) Trapping experiments conducted without scavenger (no RS) and with scavengers: *p*-benzoquinone (PBQ) for $O_2^{\bullet-}$, ethylenediaminetetraacetic acid disodium salt dihydrate (Na_2EDTA) for h^+, and isopropyl alcohol (IPA) for ·OH.

the different kinetic models can all describe the photocatalytic degradation, implying the complex nature of the reaction kinetics. Therefore, the effects of adsorbed states, intermediates, inhibition, and physicochemical phenomena within the photocatalysts must be considered to understand such complex reaction kinetics.[33] In addition, exploring the effect of the type of substance to be degraded and its concentration according to proper kinetic models (*i.e.*, Langmuir–Hinshelwood) could help to elucidate these aspects.[34,35] In all cases, the changes induced by the synthesis process on the surface of the photocatalysts make it possible to modulate the reaction rate. Among the samples thermally treated at different temperatures and times, the highest k_1 (0.051 min^{-1}) and k_2 (4.225 mg g^{-1} min^{-1}) were observed for the sample thermally treated at 375 °C for 1 h, manifesting the important role of the $BiOI/Bi_4O_5I_2$ heterostructure.

To substantiate the impact of various competing inorganic ions on the efficiency of the photocatalytic removal of nitazoxanide by the synthesized photocatalysts, additional experiments were conducted with Cl^-, NO_3^-, and PO_4^{3-} ions and the samples thermally treated at 375 °C. As shown in Fig. 6c, the presence of Cl^- and NO_3^- ions drastically hindered the photocatalytic removal of nitazoxanide. This necessitates the removal of Cl^- and NO_3^- ions before the photocatalytic treatment of water contaminated with nitazoxanide. In contrast, the PO_4^{3-} ions slightly reduced the efficiency of the photocatalytic removal of nitazoxanide with

Table 1 Kinetic parameters for the photocatalytic removal of nitazoxanide by the synthesized photocatalysts

	Pseudo-first-order			Pseudo-second-order	
Photocatalyst	k_1 (min^{-1})	$t_{1/2}$ (min)	R^2	k_2 (mg g^{-1} min^{-1})	R^2
BiI_3	0.01041	42.14307	0.95244	0.029292	0.925258
350 °C	0.01645	66.54891	0.89953	0.052519	0.956483
375 °C	0.05115	128.3145	0.75580	4.225691	0.790836
400 °C	0.01310	49.52926	0.84657	0.029078	0.942764
425 °C	0.00540	13.55094	0.96187	0.028774	0.914537
450 °C	0.00512	12.03420	0.82674	0.026824	0.893217
1 h	0.05115	128.3145	0.75580	4.225691	0.790836
3 h	0.01142	65.53	0.50838	0.07649	0.66903
5 h	0.01135	63.45	0.43380	0.06954	0.68673
7 h	0.01092	61.04	0.41180	0.05205	0.84927
9 h	0.01057	60.69	0.34705	0.04790	0.87584

respect to the absence of inorganic ions. Similar results were noted during the removal of sulfamethoxazole by ClO_2-assisted BiOI-based photocatalysis.[31] Such a dramatic effect of inorganic ions on the efficiency of the photocatalytic removal of nitazoxanide by the prepared photocatalytic materials may be explained by the change in pH, stemming from the presence of inorganic ions or the scavenging effect of ions and the formation of radicals: $HOCl^{\bullet-}$ (1.49 V, k = 6.1 ± 0.8 × 10^9 M^{-1} s^{-1}), $Cl^{\bullet}$ (2.03 V, k = 4.3 × 10^9 M^{-1} s^{-1}),[36] $NO_3^{\bullet}$ (k = 1.4 × 10^8 M^{-1} s^{-1}),[37] and $HPO_4^{\bullet-}$ (k = 8 × 10^5 M^{-1} s^{-1})[38] with lower oxidizing power than $^{\bullet}OH$ (2.8 V *vs.* NHE at pH = 0), thus reducing the efficiency of the photocatalytic activity.[39] Similarly, the efficiency of the photocatalytic removal of ritonavir was decreased by introducing Cl^-, NO_3^-, and $H_2PO_4^-$.[11] Fig. 6d shows the influence of water matrices on the efficiency of the photocatalytic removal of nitazoxanide by the synthesized samples. Apparently, the photocatalytic removal of nitazoxanide was more efficient in distilled water (DW) in comparison to tap water (TW) and treated wastewater (TWW). Although the compositions of TW and TTW significantly differ from that of DW, their efficiency in the photocatalytic removal of nitazoxanide was at least 75%. In the case of TW, the presence of Cl^- (35 mg L^{-1} according to the supplier of the TW samples), not NO_3^- (<2 mg L^{-1}), was the main reason for hindering the photocatalytic removal of nitazoxanide. The presence of dissolved organic matter and nitrogen in TTW was responsible for lowering the efficiency of the photocatalytic removal of nitazoxanide. The reusability test was conducted for the photocatalytic degradation of nitazoxanide over the BiOI/$Bi_4O_5I_2$ heterostructure for three consecutive cycles. As shown in Fig. S3,† the BiOI/$Bi_4O_5I_2$ heterostructure has good stability in the photocatalytic degradation of nitazoxanide for three consecutive cycles.

The toxicity of water samples after the photocatalytic reaction in the presence of the sample thermally treated at 375 °C was evaluated for *Aliivibrio fischeri*. As shown in Fig. 6e, the initial aqueous solution containing nitazoxanide shows the highest toxicity to *Aliivibrio fischeri* and >35% bioluminescence is inhibited. Apparently, the photocatalytic treatment reduced the toxicity, and the final aqueous solutions after photocatalytic treatment were slightly toxic, inhibiting the bioluminescence from >10 up to >25%. This confirms that the photocatalytic treatment in the presence of the synthesized photocatalysts is effective not only in the removal of nitazoxanide but also in the detoxification of wastewater. The observed inhibition of bioluminescence for the samples thermally treated at 425 °C and 450 °C possibly resulted from the formation of toxic by-products during the photodegradation of nitazoxanide since no traces of nitazoxanide were detected after the photocatalytic reaction.

In the photocatalytic process, various reactive species are involved, including photoexcited holes, hydroxyl, and superoxide radicals. To verify their impact on the photocatalytic removal of nitazoxanide by the synthesized photocatalysts, the trapping experiments were parallelly conducted using isopropyl alcohol (IPA, 1000 mg L^{-1}), *p*-benzoquinone (PBQ, 1 mg L^{-1}), and ethylenediaminetetraacetic acid disodium salt dihydrate (Na_2EDTA, 100 mg L^{-1}) as the scavengers of $^{\bullet}OH$, $O_2^{\bullet-}$, and h^+, respectively. As shown in Fig. 6f, photoexcited holes and hydroxyl radicals played an important role in the photocatalytic removal of nitazoxanide by the synthesized photocatalyst. Unlike in previous reports,[40–43] superoxide radicals were not the main driving force in the photocatalytic reaction, presumably due to the low content of $Bi_4O_5I_2$, resulting in a smaller number of the BiOI/$Bi_4O_5I_2$ heterostructures. The photocatalytic performance of the BiOI/$Bi_4O_5I_2$ heterojunctions was previously studied.[41,42] In the context of photocatalytic performance, it is noteworthy that the conduction band (CB) and valence band (VB) potentials reported for BiOI and $Bi_4O_5I_2$ in previous studies offer valuable information. BiOI exhibits more positive potentials (E_{CB} = 0.07 V *vs.* NHE and E_{VB} = 1.91 V *vs.* NHE)[42] than $Bi_4O_5I_2$, where the CB potential is negative (E_{CB} = −0.68 V *vs.* NHE),[42] although with a similar VB potential (E_{VB} = 1.78 V *vs.* NHE)[42] (Fig. 7a). It is important to recognize that, for the crystals synthesized by applying different synthesis routes, these band potential values can vary depending on various factors, including crystal structure, size, crystallinity, defects, and density of electronic states. Therefore, the synthesis method used in this work may influence these potential values. Therefore, it is prudent to consider these reported potentials as initial approximations for our analysis, which allows us to

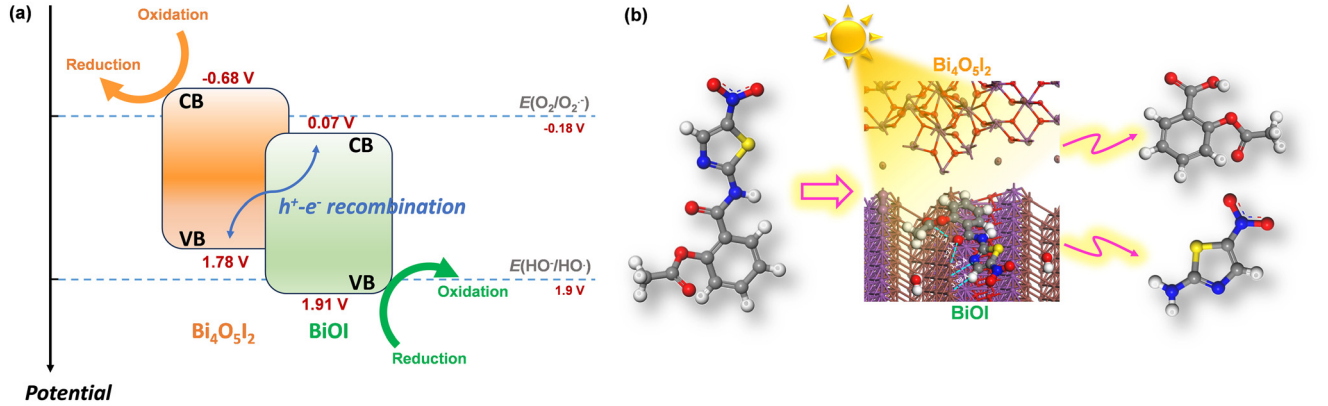

Fig. 7 (a) Band structures and redox potentials in BiOI/$Bi_4O_5I_2$ heterostructure (potentials in V *vs.* NHE at pH = 7) and (b) possible photodegradation pathways[52] of nitazoxanide by the synthesized photocatalyst.

discern relative trends. For example, the relatively positive VB potential of BiOI suggests the feasibility of oxidizing hydroxyl ions to generate hydroxyl radicals (1.9 V *vs.* NHE at pH = 7 for $HO^-/HO^{\bullet}$)[44,45] within this photocatalyst. Meanwhile, in the CB of $Bi_4O_5I_2$, the processes, such as oxygen reduction reaction (−0.18 V *vs.* NHE at pH = 7 for $O_2/O_2^{\bullet-}$)[44] and/or redox reactions associated with nitazoxanide photochemistry (Fig. 7b), can potentially complete the charge balance.[46,47]

Exploring the photoelectrochemical behavior of bismuth (oxy)iodides provides insights into the underlying mechanisms and photocatalytic processes. Fig. 8a shows the chronoamperometric (CA) response at high overpotential in several dark–light cycles. When the light is supplied, the current transiently increases for all samples studied, defining an intense peak or spikes and then decaying to a steady state value. When the light is turned off, the current tends to zero, defining a negative overshoot. This evidence is characteristic of semiconductor–electrolyte interfaces, where the so-called "band edge unpinning" occurs.[48] Therefore, surface recombination is important, and there may be some changes in the chemical composition of the interface. The electron transfer reactions are relatively slow, and the concentration of minority carriers increases to levels that modify the potential drop across the Helmholtz layer in the electrolyte.[48] The trend observed in the stationary value of the photocurrent at high overpotential follows the order: 375 °C > 350 °C > BiI_3 > 400 °C = 425 °C = 450 °C, which is in good agreement with the results of the photocatalytic kinetics study. Fig. 8b shows the lifetime during open-circuit potential decay (OCPD). The OCPD condition manifests as a scenario wherein the PEC response of the interface tends to a low overpotential.[25] Therefore, behaviors can be differentiated due to the differences in the recombination processes.[26] In fact, the sample thermally treated at 375 °C exhibits higher lifetime values for lower potentials compared to other samples. For all samples studied, the trend of the semilogarithmic graph of lifetime *versus* open-circuit potential is linear, which is consistent with an electron transfer theory.[49] A longer lifetime suggests a slower recombination rate, which infers a greater availability of charge carriers for photocurrent collection.[33] Therefore, the PEC results support the idea that electron transfer increases

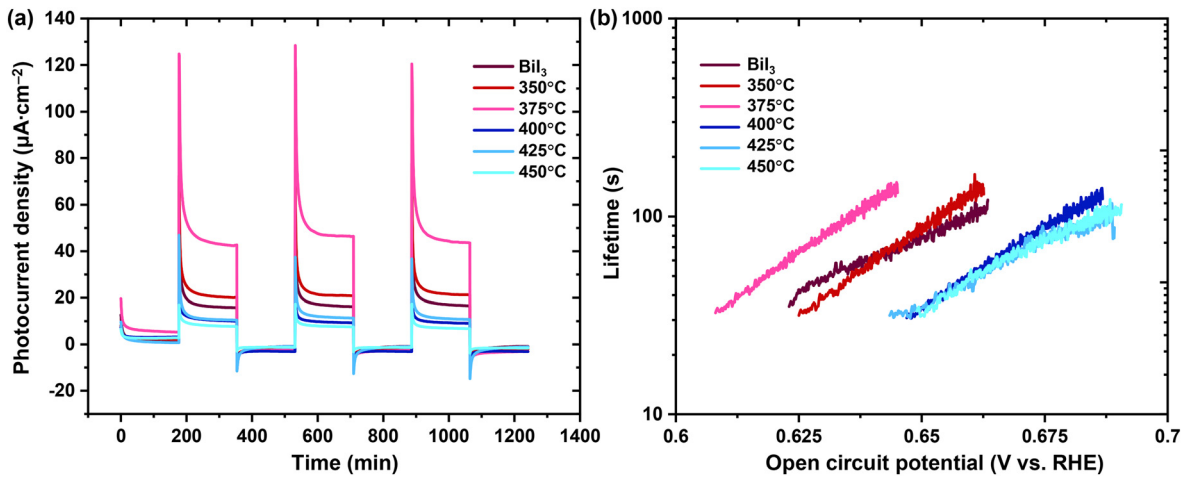

Fig. 8 Results of photoelectrochemical measurements: (a) CA at 1.8 V *vs.* RHE and (b) lifetime *vs.* open-circuit potential.

at the expense of recombination, and the $BiOI/Bi_4O_5I_2$ heterojunction formed in the sample thermally treated at 375 °C results in a higher photocurrent at high overpotential and longer lifetimes during deactivation under OCPD conditions. It is worth noting that the surface photoredox reactions and photocorrosion are the processes that require further investigations through comprehensive PEC studies.[50,51]

The chemical structure of nitazoxanide contains hydrogen-bonding acceptor sites: the O atom in the ester and $-NO_2$ capable of forming N–O···H with the solvent molecules and the N atom in the –NH groups capable of forming N–H···O bonds.[23] The $-NO_2$ and –NH groups are the principal sites of electrophilic and nucleophilic attacks on the nitazoxanide molecule, respectively.[23] The presence of conjugated double bonds and nitro and amide groups being chromophores indicates that the nitazoxanide molecule should be susceptible to light.[24] During the photocatalytic process, the nitazoxanide molecule underwent decomposition *via* hydrolysis into acetylsalicylic acid (1) and the respective aminonitrothiazol (2) (Fig. 7b). In the MS analysis, the appearance of a fragment at m/z = 266 confirmed the deacetylation process, which was followed by the cleavage of the amide according to the fragment at m/z = 121. The fragment at m/z = 163 indicated the cleavage of the amide without the deacetylation process.[52] The formed acetylsalicylic acids underwent further oxidation, which led to the formation of the ring-opening products due to the cleavage of a C–C bond (with a cyclopentane-1,3-dione core). Further decarboxylation (ascribed to the photo-Kolbe reaction) that is initiated by hole oxidation of the carboxylic acids resulted in the release of CO_2 and radicals.

The adsorption of molecules on the photocatalyst surface is an important step for heterogeneous photocatalysis. To gain insights into the photodegradation of nitazoxanide in aqueous solution, its adsorption was studied using numerical molecular dynamics (MD) simulations and stochastic Monte Carlo (MC) simulations.[53] In these MD and MC simulations, the interaction among the nitazoxanide and water molecules was taken into account as forces and energy changes related to the random movement of the components, respectively. The MD simulation of nitazoxanide in an aqueous solution was performed by Forcite and Adsorption Locator modules in Materials Studio (BIOVIA). The detailed methodology for the modelling was described elsewhere,[54,55] and the crystallographic CIF files for BiI_3, BiOI, $Bi_4O_5I_2$, and Bi_5O_7I (ref. 56–59) were used. Their predominant crystallographic planes were chosen for modelling according to the XRD and TEM data. The affinities of nitazoxanide and water molecules were evaluated through the distribution field density, adsorption energy (E_{ads}), and differential adsorption dE_{ad}/dN_i of the components (Table S2†). The E_{ads} values of the nitazoxanide model are much higher on the BiOI surface than the E_{ads} values on the BiI_3, $Bi_4O_5I_2$, and Bi_5O_7I surfaces in the following order: −138.92 kcal mol^{-1} for BiOI (1 0 2) > −46.81 kcal mol^{-1} for $Bi_4O_5I_2$ ($\bar{1}$ 0 1) > −43.61 kcal mol^{-1} for Bi_5O_7I (2 0 0) > −42.94 kcal mol^{-1} for BiI_3 (2 $\bar{1}$ 3).

According to the data shown in Table S2,† the water molecules have a better affinity for the BiOI surface than for the BiI_3, $Bi_4O_5I_2$, and Bi_5O_7I surfaces. The calculated E_{ads} values for the crystallographic planes of BiOI are different and significantly exceeded the similar values for BiI_3, $Bi_4O_5I_2$, and Bi_5O_7I in the following order: −138.92 kcal mol^{-1} for BiOI (1 0 2) > −124.54 kcal mol^{-1} for BiOI (1 1 0) > −122.20 kcal mol^{-1} for BiOI (1 $\bar{1}$ 0). The experimental data and degradation constants (k_1 and k_2) showed that the BiOI and $Bi_4O_5I_2$ has a higher photocatalytic activity for the degradation of nitazoxanide than individual $Bi_4O_5I_2$ and BiOI (Table 1). Considering the localization of the nitazoxanide and water molecules at the interface formed between two predominant crystallographic planes of BiOI and $Bi_4O_5I_2$, it was found that the adsorption of nitazoxanide molecules has a preference on the BiOI surface (Fig. 9a) *via* the formation of a network of close contacts (<3.5 Å) between nitazoxanide molecules and iodine atoms (Fig. 9b). This leads to the re-distribution of field density near BiOI (1 1 0) away from $Bi_4O_5I_2$ ($\bar{1}$ 0 1). The high photocatalytic activity of $BiOI/Bi_4O_5I_2$ is correlated to its higher adsorption than that of $Bi_4O_5I_2$ but is similar to BiOI according to the data for the adsorption energy (Fig. 9b) and differential adsorption energy of nitazoxanide and water molecules (Fig. 9c) on different

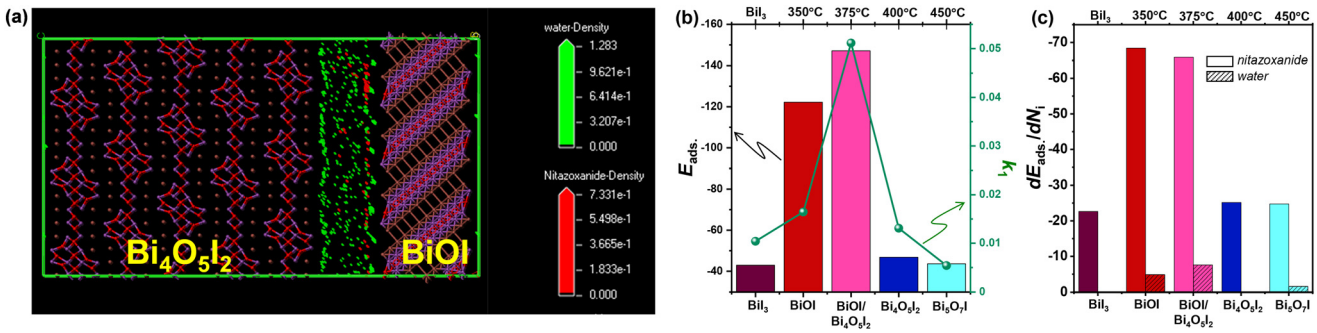

Fig. 9 (a) Visualization of adsorption of nitazoxanide and water molecules onto the $BiOI/Bi_4O_5I_2$ interface. The red, violet, and brown spheres represent oxygens, bismuth, and iodine. Isosurface field density: green is water and red is nitazoxanide. (b) Effect of adsorption energy on degradation constants for different bismuth (oxy)iodide phases. (c) Differential adsorption energy of nitazoxanide and water molecules on different bismuth (oxy)iodide phases.

crystallographic planes (Table S2†). This confirms that the incorporation of BiOI can enhance the photocatalytic activity of $Bi_4O_5I_2$ for the degradation of nitazoxanide.

4. Conclusions

To sum up, the effect of thermal treatment on the phase transition from bismuth iodide to bismuth oxyiodides was studied at temperatures ranging from 350 °C to 450 °C. Compared with thermal treatment time, the thermal treatment temperature showed a more pronounced effect on phase transition, resulting in the formation of different bismuth oxyiodide crystalline phases with varying optoelectronic properties and photocatalytic activity. Thermal treatment at 375 °C for 1 h led to the formation of the BiOI/$Bi_4O_5I_2$ heterostructure, which exhibited the highest photocatalytic activity for the degradation of nitazoxanide, with respective rate constants of k_1 (0.051 min^{-1}) and k_2 (4.225 mg g^{-1} min^{-1}), highlighting the importance of the presence of multiple phases based on bismuth oxyiodides. Trapping experiments confirmed the involvement of photoexcited holes and hydroxyl radicals as the major reactive species in the photodegradation of nitazoxanide. The results of photoelectrochemical measurements showed that the electron transfer and recombination processes are inversely linked in the sample with the BiOI/$Bi_4O_5I_2$ heterojunction. The photodegradation of nitazoxanide proceeded *via* hydrolysis into acetylsalicylic acid and the respective aminonitrothiazol, which were followed by the deacetylation and decarboxylation processes. According to the MD simulation, the high photocatalytic activity of BiOI/$Bi_4O_5I_2$ is correlated to its higher adsorption. The toxicity test conducted with *Aliivibrio fischeri* revealed that the BiOI/$Bi_4O_5I_2$ heterostructure is effective not only in the removal of nitazoxanide but also in the detoxification of wastewater, demonstrating its potential for practical application in the wastewater treatment process.

Author contributions

Mirabbos Hojamberdiev: conceptualization, investigation, methodology, validation, visualization, writing – original draft, writing – review & editing; Ronald Vargas: formal analysis, investigation, software, validation, writing – original draft, writing – review & editing; Lorean Madriz: formal analysis, investigation, software, validation, writing – original draft, writing – review & editing; Kunio Yubuta: formal analysis, investigation, software, validation, writing – original draft; Zukhra C. Kadirova – formal analysis, investigation, software, validation, writing – original draft; Ulugbek Shaislamov – formal analysis, investigation, software, validation, writing – original draft; Lokesh Koodlur Sannegowda: investigation, writing – review & editing; Katarzyna Jędruchniewicz: formal analysis, investigation, software, validation, writing – original draft; Rafał Typek: formal analysis, investigation, software, validation, writing – original draft; Katsuya Teshima: formal analysis, investigation, software, validation, writing – original draft; Bożena Czech: conceptualization, investigation, methodology, supervision, validation, visualization, writing – original draft, writing – review & editing.

Conflicts of interest

There are no conflicts to declare.

Acknowledgements

MPWIK Lublin is acknowledged for providing wastewater samples. The authors gratefully acknowledge the use of services and facilities of The John Paul II Catholic University of Lublin, Poland, co-funded by the European Regional Development Fund (POPW.01.03.00-06-003/09-00). The India-Uzbekistan Collaborative Grants (no. INT/Uzbek/P-21 and UZB-Ind-2021-91) are also acknowledged. The authors thank Ms. Reiko Shiozawa from Shinshu University, Japan, for her kind assistance in the XPS analysis.

References

1 I. A. Al-Baldawi, A. A. Mohammed, Z. H. Mutar, S. R. S. Abdullah, S. S. Jasim, A. F. Almansoory and N. I. Ismail, Application of phytotechnology in alleviating pharmaceuticals and personal care products (PPCPs) in wastewater: Source, impacts, treatment, mechanisms, fate, and SWOT analysis, *J. Cleaner Prod.*, 2021, **319**, 128584.

2 L. F. Angeles, R. A. Mullen, I. J. Huang, C. Wilson, W. Khunjar, H. I. Sirotkin, A. E. McElroy and D. S. Aga, Assessing pharmaceutical removal and reduction in toxicity provided by advanced wastewater treatment systems, *Environ. Sci.: Water Res. Technol.*, 2020, **6**, 62–77.

3 A. Sengar and A. Vijayanandan, Human health and ecological risk assessment of 98 pharmaceuticals and personal care products (PPCPs) detected in Indian surface and wastewaters, *Sci. Total Environ.*, 2022, **807**, 150677.

4 J. He, T. Feng, L. Tao, Y.-E. Peng, L. Tong, X.-W. Zhao, X. Shao, L.-Y. Xu, Y.-L. Yang and Y.-B. Zhao, Distribution and impacts on the geological environment of antiviral drugs in major waters of Wuhan, China, *China Geol.*, 2022, **5**, 402–410.

5 L.-A. Phan Thi, S. C. Panchangam, H.-T. Dod and V.-H. Nguyen, Prospects and challenges of photocatalysis for degradation and mineralization of antiviral drugs, in *Nanostructured Photocatalysts: From Fundamental to Practical Applications*, ed. V.-H. Nguyen, D.-V. N. Vo and S. Nanda, Elsevier, 2021, pp. 489–517.

6 S. Jain, P. Kumar, R. K. Vyas, P. Pandit and A. K. Dalai, Occurrence and Removal of Antiviral Drugs in Environment: A Review, *Water, Air, Soil Pollut.*, 2013, **224**, 1410.

7 C. Prasse, M. P. Schlüsener, R. Schulz and T. A. Ternes, Antiviral Drugs in Wastewater and Surface Waters: A New Pharmaceutical Class of Environmental Relevance?, *Environ. Sci. Technol.*, 2010, **44**, 1728–1735.

8 J. Meijide, G. Lama, M. Pazos, M. A. Sanromán and P. S. M. Dunlop, Ultraviolet-based heterogeneous advanced oxidation processes as technologies to remove pharmaceuticals from wastewater: An overview, *J. Environ. Chem. Eng.*, 2022, **10**, 107630.

9 M. Hojamberdiev, B. Czech, A. C. Göktaş, K. Yubuta and Z. C. Kadirova, SnO_2@ZnS photocatalyst with enhanced photocatalytic activity for the degradation of selected pharmaceuticals and personal care products in model wastewater, *J. Alloys Compd.*, 2020, **827**, 154339.

10 B. Czech, P. Zygmunt, Z. C. Kadirova, K. Yubuta and M. Hojamberdiev, Effective photocatalytic removal of selected pharmaceuticals and personal care products by elsmoreite/tungsten oxide@ZnS photocatalyst, *J. Environ. Manage.*, 2020, **270**, 110870.

11 M. Hojamberdiev, B. Czech, A. Wasilewska, A. Boguszewska-Czubara, K. Yubuta, H. Wagata, S. S. Daminova, Z. C. Kadirova and R. Vargas, Detoxifying SARS-CoV-2 antiviral drugs from model and real wastewaters by industrial waste-derived multiphase photocatalysts, *J. Hazard. Mater.*, 2022, **429**, 128300.

12 B. Czech, A. Krzyszczak, A. Boguszewska-Czubara, G. Opielak, I. Jośko and M. Hojamberdiev, Revealing the toxicity of lopinavir- and ritonavir-containing water and wastewater treated by photo-induced processes to Danio rerio and Aliivibrio fischeri, *Sci. Total Environ.*, 2022, **824**, 153967.

13 W.-L. Wang, Q.-Y. Wu, Z.-M. Wang, H.-Y. Hu, N. Negishi and M. Torimura, Photocatalytic degradation of the antiviral drug Tamiflu by UV-A/TiO_2: Kinetics and mechanisms, *Chemosphere*, 2015, **131**, 41–47.

14 A. H. Asif, S. Wang and H. Sun, Hematite-based nanomaterials for photocatalytic degradation of pharmaceuticals and personal care products (PPCPs): A short review, *Curr. Opin. Green Sustainable Chem.*, 2021, **28**, 100447.

15 N. Tian, C. Hu, J. Wang, Y. Zhang, T. Ma and H. Huang, Layered bismuth-based photocatalysts, *Coord. Chem. Rev.*, 2022, **463**, 214515.

16 J. Han, G. Zhu, M. Hojamberdiev, J. Peng and P. Liu, Temperature effect on phase transition and morphological transformation of BiOI microspheres to Bi_5O_7I microstructures, *Mater. Lett.*, 2016, **169**, 122–125.

17 L. Zhang, H. Wang, Z. Chen, P. K. Wong and J. Liu, Bi_2WO_6 micro/nano-structures: Synthesis, modifications and visible-light-driven photocatalytic applications, *Appl. Catal., B*, 2011, **106**, 1–13.

18 M. Hojamberdiev, Z. C. Kadirova, E. Zahedi, D. Onna, M. C. Marchi, G. Zhu, N. Matsushita, M. Hasegawa, S. Aldabe Bilmes and K. Okada, Tuning the morphological structure, light absorption, and photocatalytic activity of Bi_2WO_6 and Bi_2WO_6-BiOCl through cerium doping, *Arabian J. Chem.*, 2020, **13**, 2844–2857.

19 B. Czech and M. Hojamberdiev, UVA- and visible-light-driven photocatalytic activity of three-layer perovskite Dion-Jacobson phase $CsBa_2M_3O_{10}$ (M = Ta, Nb) and oxynitride crystals in the removal of caffeine from model wastewater, *J. Photochem. Photobiol., A*, 2016, **324**, 70–80.

20 H. Liu, J. Cai, M. Luo, C. Chen and P. Hu, Novel mesoporous bismuth oxyiodide single crystal nanosheets with enhanced catalytic activity, *RSC Adv.*, 2020, **10**, 5913–5918.

21 L. Ye, L. Tian, T. Peng and L. Zan, Synthesis of highly symmetrical BiOI single-crystal nanosheets and their {001} facet-dependent photoactivity, *J. Mater. Chem.*, 2011, **21**, 12479–12484.

22 N. Chandiwana, C. Kruger, H. Johnstone, M. F. Chughlay, C. Ju, B. Kim, Y. Dineka, S. Arbe-Barnes, R. Miller, A. Owen, A. Hill, D. Windgassen, N. Abla, A. C. Marrast, S. Duparc and W. D. F. Venter, Safety and efficacy of four drug regimens versus standard-of-care for the trea14049tment of symptomatic outpatients with COVID-19: A randomised, open-label, multi-arm, phase 2 clinical trial, *EBioMedicine*, 2022, **86**, 104322.

23 Y. Li, C. Li, X. Gao and H. Lv, Nitazoxanide in aqueous co-solvent solutions of isopropanol/DMF/NMP: Solubility, solvation thermodynamics and intermolecular interactions, *J. Chem. Thermodyn.*, 2023, **176**, 106928.

24 M. D. Malesuik, H. M. L. Gonçalves, C. S. Paim, E. E. S. Schapoval and M. Steppe, LC: Analysis of Photodegradation Kinetics of Nitazoxanide in Pharmaceutical Formulations, *J. Chromatogr. Sci.*, 2009, **47**, 745–748.

25 R. Vargas, L. Madriz, V. Márquez, D. Torres, Z. C. Kadirova, K. Yubuta and M. Hojamberdiev, Elucidating the enhanced photoelectrochemical performance of zinc-blende ZnS/wurtzite ZnO heterojunction and adsorption of water molecules by molecular dynamics simulations, *Mater. Sci. Semicond. Process.*, 2022, **142**, 106494.

26 J. Bisquert, A. Zaban, M. Greenshtein and I. Mora-Seró, Determination of Rate Constants for Charge Transfer and the Distribution of Semiconductor and Electrolyte Electronic Energy Levels in Dye-Sensitized Solar Cells by Open-Circuit Photovoltage Decay Method, *J. Am. Chem. Soc.*, 2004, **126**, 13550–13559.

27 C. M. Domínguez, P. Ventura, A. Checa-Fernández and A. Santos, Comprehensive study of acute toxicity using Microtox® bioassay in soils contaminated by lindane wastes, *Sci. Total Environ.*, 2023, **856**, 159146.

28 X. Xiao, Y. Lin, B. Pan, W. Fan and Y. Huang, Photocatalytic degradation of methyl orange by BiOI/$Bi_4O_5I_2$ microspheres under visible light irradiation, *Inorg. Chem. Commun.*, 2018, **93**, 65–68.

29 T. Wang, C. Zhao, L. Meng, Y. Li, H. Chu, F. Wang, Y. Tao, W. Liu and C. C. Wang, In-situ-construction of BiOI/UiO-66 heterostructure via nanoplate-on-octahedron: A novel p-n heterojunction photocatalyst for efficient sulfadiazine elimination, *Chem. Eng. J.*, 2023, **451**, 138624.

30 B. O. Orimolade and O. A. Arotiba, Enhanced photoelectrocatalytic degradation of diclofenac sodium using a system of Ag-$BiVO_4$/BiOI anode and Ag-BiOI cathode, *Sci. Rep.*, 2022, **12**, 4214.

31 X. Song, R. Su, Y. Wang, Y. Zhang, B. Gao, Y. Wang, D. Ma and Q. Li, Visible light-driven chlorite activation process for

enhanced sulfamethoxazole antibiotics degradation, antimicrobial resistance reduction and biotoxicity elimination, *Chem. Eng. J.*, 2023, **452**, 139103.

32 J. Xu, Q. Zhang, X. Gao, P. Wang, H. Che, C. Tang and Y. Ao, Highly Efficient Fe^{III}-initiated Self-cycled Fenton System in Piezo-catalytic Process for Organic Pollutants Degradation, *Angew. Chem.*, 2023, **135**, e202307018.

33 O. Núñez and R. Vargas, The interplay between RedOx, photophysics and surface process in Bi_2WO_6 photocatalyst, in *A Closer Look at Chemical Kinetics*, ed. V. Martinez-Luaces, Nova Science Publishers, New York, USA, 2023.

34 A. Mills, C. O'Rourke and K. Moore, Powder semiconductor photocatalysis in aqueous solution: An overview of kinetics-based reaction mechanisms, *J. Photochem. Photobiol., A*, 2015, **310**, 66–105.

35 R. Vargas, D. Carvajal, L. Madriz and B. R. Scharifker, Chemical kinetics in solar to chemical energy conversion: The photoelectrochemical oxygen transfer reaction, *Energy Rep.*, 2020, **6**, 2–12.

36 T. Peng, C. Xu, L. Yang, B. Yang, W.-W. Cai, F. Gu and G.-G. Ying, Kinetics and Mechanism of Degradation of Reactive Radical-Mediated Probe Compounds by the UV/Chlorine Process: Theoretical Calculation and Experimental Verification, *ACS Omega*, 2022, **7**, 5053–5063.

37 S. P. Mezyk, T. D. Cullen, K. A. Rickman and B. J. Mincher, The Reactivity of the Nitrate Radical ($^{\bullet}NO_3$) in Aqueous and Organic Solutions, *Int. J. Chem. Kinet.*, 2017, **49**, 635–642.

38 P. Maruthamuthu and P. Neta, Phosphate radicals. Spectra, acid-base equilibriums, and reactions with inorganic compounds, *J. Phys. Chem.*, 1978, **82**, 710–713.

39 M. Carballa, F. Omil, T. Ternes and J. M. Lema, Fate of pharmaceutical and personal care products (PPCPs) during anaerobic digestion of sewage sludge, *Water Res.*, 2007, **41**, 2139–2150.

40 M. Sun, Q. Wei, Y. Shao, B. Du, T. Yan, L. Yan and D. Li, Engineering composition-tunable 3D hierarchical bismuth oxyiodides heterojunctions: Ionic liquid-assisted fabrication with strong adsorption ability and enhanced photocatalytic properties, *Appl. Catal., B*, 2018, **233**, 250–259.

41 H. Ding, A. H. Zahid and Q. Han, Synthesis of 3D flowerlike S-scheme $Bi_4O_5I_2$/BiOI heterojunction with synergistic effect of adsorption and photocatalysis, *Mater. Sci. Eng., B*, 2023, **289**, 116209.

42 H. Cheng, J. Wu, F. Tian, L. Zhao, Z. Ji, F. Li, Q. Li, Z. Guan and T. Zhou, In-situ crystallization for fabrication of BiOI/$Bi_4O_5I_2$ heterojunction for enhanced visible-light photocatalytic performance, *Mater. Lett.*, 2018, **232**, 191–195.

43 Y.-H. Cheng, J. Chen, H.-N. Che, Y.-H. Ao and B. Liu, Ultrafast photocatalytic degradation of nitenpyram by 2D ultrathin Bi_2WO_6: mechanism, pathways and environmental factors, *Rare Met.*, 2022, **41**, 2439–2452.

44 D. A. Armstrong, R. E. Huie, W. H. Koppenol, S. V. Lymar, G. Merényi, P. Neta, B. Ruscic, D. M. Stanbury, S. Steenken and P. Wardman, Standard electrode potentials involving radicals in aqueous solution: inorganic radicals (IUPAC Technical Report), *Pure Appl. Chem.*, 2015, **87**, 1139–1150.

45 L. S. Gómez-Velázquez, L. Madriz, M. Rigoletto, E. Laurenti, M. Bizarro, M. L. Dell'Arciprete and M. C. González, Structural and Physicochemical Properties of Carbon Nitride Nanoparticles via Precursor Thermal Treatment: Effect on Methyl Orange Photocatalytic Discoloration, *ACS Appl. Nano Mater.*, 2023, **6**, 14049–14062.

46 G. X. Castillo-Cabrera, P. J. Espinoza-Montero, P. Alulema-Pullupaxi, J. R. Mora and M. H. Villacís-García, Bismuth Oxyhalide-Based Materials (BiOX: X = Cl, Br, I) and Their Application in Photoelectrocatalytic Degradation of Organic Pollutants in Water: A Review, *Front. Chem.*, 2022, **10**, 900622.

47 O. Núñez, L. Madriz, D. Carvajal, J. Tatá and R. Vargas, Unprecedented large solvent (H_2O vs D_2O) isotope effect in semiconductors photooxidation, *J. Phys. Org. Chem.*, 2019, **32**, e3952.

48 L. M. Peter, A. B. Walker, T. Bein, A. G. Hufnagel and I. Kondofersky, Interpretation of photocurrent transients at semiconductor electrodes: Effects of band-edge unpinning, *J. Electroanal. Chem.*, 2020, **872**, 114234.

49 B. Liu, X. Zhao, C. Terashima, A. Fujishima and K. Nakata, Thermodynamic and kinetic analysis of heterogeneous photocatalysis for semiconductor systems, *Phys. Chem. Chem. Phys.*, 2014, **16**, 8751–8760.

50 L. M. Peter, E. A. Ponomared and D. J. Fermín, Intensity-modulated photocurrent spectroscopy: reconciliation of phenomenological analysis with multistep electron transfer mechanisms, *J. Electroanal. Chem.*, 1997, **427**, 79–96.

51 F. E. Bedoya-Lora, I. Holmes-Gentle and A. Hankin, Electrochemical techniques for photoelectrode characterisation, *Curr. Opin. Green Sustain. Chem.*, 2021, **29**, 100463.

52 F. Barbosa, L. Pezzi, J. Sorrentino, M. Steppe, N. Volpato and A. S. L. Mendez, pH effect on stability and kinetics degradation of nitazoxanide in solution, *Drug Anal. Res.*, 2020, **4**, 12–17.

53 F. Müller, H. Christiansen, S. Schnabel and W. Janke, Fast, Hierarchical, and Adaptive Algorithm for Metropolis Monte Carlo Simulations of Long-Range Interacting Systems, *Phys. Rev. X*, 2023, **13**, 031006.

54 M. Hojamberdiev, Z. C. Kadirova, Y. Makinose, G. Zhu, N. Matsushita, J. Rodríguez, S. Aldabe Bilmes, M. Hasegawa and K. Okada, Influence of BiOI content on the photocatalytic activity of Bi_2WO_6/BiOI/allophane composites and molecular modeling studies of acetaldehyde adsorption, *J. Taiwan Inst. Chem. Eng.*, 2017, **81**, 258–264.

55 M. Hojamberdiev, Z. C. Kadirova, R. V. Gonçalves, K. Yubuta, N. Matsushita, K. Teshima, M. Hasegawa and K. Okada, Reduced graphene oxide-modified Bi_2WO_6/BiOI composite for the effective photocatalytic removal of organic pollutants and molecular modeling of adsorption, *J. Mol. Liq.*, 2018, **268**, 715–727.

56 E. Keller and V. Krämer, A Strong Deviation from Vegard's Rule: X-Ray Powder Investigations of the Three Quasi-Binary

Phase Systems BiOX–BiOY (X, Y = Cl, Br, I), *Z. Naturforsch., B: J. Chem. Sci.*, 2005, **60**, 1255–1263.
57 E. Keller, V. Krämer, M. Schmidt and H. Oppermann, The crystal structure of $Bi_4O_5I_2$ and its relation to the structure of $Bi_4O_5Br_2$, *Z. Kristallogr.*, 2002, **217**, 256–264.
58 U. Eggenweiler, J. Ketterer, E. Keller and V. Krämer, The crystal structure of α-Bi_5O_7I, *Z. Kristallogr.*, 2001, **216**, 230–233.
59 M. Ruck, Darstellung und Kristallstruktur von fehlordnungsfreiem Bismuttriiodid, *Z. Kristallogr.*, 1995, **210**, 650–655.

